

The 22 May 2007 B-class flare: new insights from *Hinode* observations

G. Del Zanna¹, U. Mitra-Kraev¹, S. J. Bradshaw^{2,3,4}, H. E. Mason¹, and A. Asai^{5,6}

¹ DAMTP, Centre for Mathematical Sciences, Wilberforce Road, Cambridge, CB3 0WA, UK
 e-mail: g.del-zanna@damtp.cam.ac.uk

² NASA Goddard Space Flight Center, Solar Physics Lab., Code 671, 8800 Greenbelt Road, Greenbelt, MD 20771, USA

³ Dept. of Computational and Data Sciences, George Mason University, 4400 University Drive, MSN 6A2, Fairfax, VA 22030, USA

⁴ Department of Physics and Astronomy, Rice University, Houston, TX 77005, USA

⁵ Nobeyama Solar Radio Observatory, National Astronomical Observatory of Japan, Minamisaku, Nagano 384-1305, Japan

⁶ Unit of Synergetic Studies for Space, Kyoto University, Yamashina, Kyoto 607-8471, Japan

Received 30 April 2010 / Accepted 9 October 2010

ABSTRACT

We present multi-wavelength observations of a small B-class flare which occurred on the Sun on 2007 May 22. The observations include data from *Hinode*, GOES, TRACE and the Nobeyama Radioheliograph. We obtained spatially and spectrally-resolved information from the *Hinode* EUV Imaging Spectrometer (EIS) during this event. The temporal and temperature coverage of the EIS observations provides new insights into our understanding of chromospheric evaporation and cooling. The flare showed many “typical” features, such as brightenings in the ribbons, hot (10 MK) loop emission and subsequent cooling. We also observed a new feature, strong (up to 170 km s^{-1}) blue-shifted emission in lines formed around 2–3 MK, located at the footpoints of the 10 MK coronal emission and within the ribbons. Electron densities at 2 MK in the kernels are high, of the order of 10^{11} cm^{-3} , suggesting a very narrow layer where the chromospheric evaporation occurs. We have run a non-equilibrium hydrodynamic numerical simulation using the HYDRAD code to study the cooling of the 10 MK plasma, finding good agreement between the predicted and observed temperatures, densities and ion populations. Line blending for some potentially useful diagnostic lines for flares, which are observed with *Hinode*/EIS, is also discussed.

Key words. techniques: spectroscopic – Sun: flares

1. Introduction

In order to understand which physical processes are at work during a solar flare, one useful approach is to study the mechanisms that replenish/empty the loops (e.g. evaporation and condensation), as well as the processes that create the ribbons (thermal conduction, bremsstrahlung of energetic particles). In this paper, we are interested in studying the characteristics of the source regions of chromospheric evaporation, and also how the flare plasma cools. One of the limitations in testing theoretical predictions of chromospheric evaporation and cooling has been a lack of spectroscopic measurements that cover a broad range of temperatures during the lifetime of a flare with sufficient spatial resolution. Earlier observations have been performed with various instruments, but there were limitations mainly in their spatial capability. Blue-shifted components of a few hundred km s^{-1} have been reported in the X-ray wavelength range from SOLFLEX (cf. [Doscsek et al. 1979](#)), the Solar Maximum Mission (SMM) X-ray polychromator (XRP) Bent Crystal Spectrometer (BCS) (cf. [Antonucci et al. 1982](#)), and from the Bragg Crystal Spectrometer (BCS) on YOHKOH (see, e.g., [Bentley et al. 1994](#)). The observations were mainly of H- and He-like lines (in particular Ca XIX), which are formed over a very broad range of temperatures, 8–25 MK ($1 \text{ MK} = 1 \times 10^6 \text{ K}$). The Ca XIX line profile was found to be dominated by a component with a centroid position close to rest, contrary to what predicted by 1-D hydrodynamical modelling of single loop structures (see, e.g., [Cheng et al. 1983](#)), that the whole spectral line

profile should be Doppler-shifted by a few hundred km s^{-1} . One common explanation is that the strong stationary component originates from the overlying loop structures, however the fact that it is present very early during the impulsive phase is puzzling. The blue-shifted component was thought to be located at the footpoints of X-ray loops and to be driven by non-thermal electrons accelerated during the primary energy release ([Antonucci et al. 1984](#)). A possible solution to the puzzle is that flare loops are composed of sub-resolution structures (see [Doscsek & Warren 2005](#), and references therein).

The blue-shifts are thought to be a signature of the evaporation of chromospheric plasma caused by an overpressure, due to sudden heating produced by collisions of non-thermal electrons (originating in the corona) with the ambient plasma in the upper layers of the chromosphere, and by the heat conducted from the corona, once high-temperatures are reached there. Numerical simulations indicate that the amount and velocity of the chromospheric plasma evaporated to coronal temperatures depends on the energy flux of the non-thermal electrons. Also, depending on the amount of energy, the overpressure, besides the evaporation, can drive observable downward-moving plasma at chromospheric temperatures. For details see, e.g., [Fisher et al. \(1985b,a\)](#); [Fisher \(1987\)](#); [Mariska et al. \(1989\)](#).

One important exception in terms of spatial resolution were the SMM Ultraviolet Spectrometer and Polarimeter (UVSP) observations of the Fe XXI line at 1354.1 Å emitted at about 10^7 K . [Mason et al. \(1986\)](#) obtained indications of blue-wing

asymmetries in the Fe XXI emitting plasma in excess of 200 km s^{-1} , in small kernels (the UVSP instrument had a spatial resolution down to $3''$).

Blue-wing asymmetries in cooler lines were also observed with the SMM XRP Flat Crystal Spectrometer (FCS) and reported by Zarro et al. (1988). Spatially-confined Mg XI blue-shifted emission during the impulsive phase of a small flare were found. Mg XI is formed in ionisation equilibrium at temperatures between 1.2 and 6 MK, i.e. much lower than Ca XIX. The SMM XRP FCS had a very limited (by today's standards) spatial resolution ($14''$), considering that kernels of chromospheric evaporation have been observed to be only a few arcseconds at most (Del Zanna et al. 2002a, 2006a).

In the past decade, SOHO has given us the opportunity to study solar flares in more detail, in particular with the Coronal Diagnostic Spectrometer (CDS). Various observations of large-scale two-ribbon flares have been carried out. For example, Czakowska et al. (1999) and Del Zanna et al. (2006b) reported SOHO/CDS observations of arcade of hot loops during the gradual phase of two large flares (the second was the X17 flare of 2003 October 28). Both papers reported strong blue-shifts in hot Fe XVI (3 MK) and Fe XIX (9 MK) lines located at the outer edges of the flare ribbons. Some observations of large flares observed with *Hinode* have also been reported (see, e.g., the review of Harra 2008).

In this paper, we are particularly interested in small flares, because their entire evolution can be studied in detail within the EIS field-of-view. The first spatially-resolved spectral observations of the entire evolution of a small flare were performed with CDS and reported by Del Zanna et al. (2002a). Long-lasting (over an hour) blue-shifts of 30 km s^{-1} in coronal lines (Mg X, Si XII, emitted at 1–2 MK) were observed. They were localised in space (a few arc seconds), and found at the footpoints of a small loop system which was very bright in Fe XIX (9 MK) emission. The blue-shifts were clearly associated with gentle chromospheric evaporation filling the coronal loops.

Del Zanna et al. (2006a) found strong blue-shifts in CDS coronal lines in some flare kernels during the impulsive phase of an M1 class flare observed on 2002 October 22. The blue-shifts were observed in regions where the coronal/flare line intensities were very weak. These observations confirmed what was expected from theory, i.e. it was found that upflows in the flare kernels were progressively larger at higher temperatures, reaching 140 km s^{-1} for Fe XIX (9 MK). Small downflows in the cooler lines were also observed. The line profiles were shifted towards the blue in Fe XIX, but the widths were large, indicating the existence of turbulent velocities.

Raftery et al. (2009) also found upflows in Fe XIX during the impulsive phase of a GOES C3-class flare observed by CDS and other instruments, although the magnitude was “only” about 80 km s^{-1} . Raftery et al. (2009) produced the first extensive study of a flare evolution using spectroscopy in conjunction with a 0-D hydrodynamic model (EBTEL). They found that thermal conduction was the dominant energy loss mechanism and the cause of gentle chromospheric evaporation during the initial 300 s of the decay phase.

The *Hinode* EUV Imaging Spectrometer (EIS, see Culhane et al. 2007) covers two wavelength bands (SW: 166–212 Å; LW: 245–291 Å) and extends the CDS capabilities in that higher-temperature emission lines from Fe XXIII and Fe XXIV can be observed. The lines observed by EIS are also individually formed over narrower temperature ranges (see Fig. 1 below), unlike the H- and He-like lines, hence are better for temperature

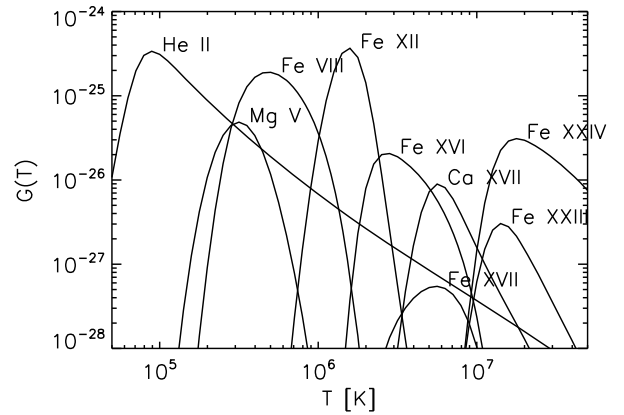


Fig. 1. Contribution functions for a selection of *Hinode*/EIS lines used in the present study (from CHIANTI v. 6, Dere et al. 2009).

diagnostics (although direct temperature measurements are not readily available for flares).

To study small scale transient phenomena in active regions at coronal and transition region temperatures, we at Cambridge (see Chifor 2008) designed a series of EIS observing sequences (named CAM_ARTB_RHESSI). The sequences have been run successfully over several active regions since April 2007 and two flares have been observed. Notice that EIS observations during the evolution of a flare are a rare event. One of the two observed cases was a moderately sized flare (GOES C1.1 class) which occurred on 2007 December 14. Milligan & Dennis (2009) presented a preliminary analysis of the impulsive phase of that flare. At one footpoint location, they found a strong stationary component in Fe XXIII and Fe XXIV lines, and significant blue-wing components with velocities of about 200 km s^{-1} , which is at odds with what is expected from theory (which predicts that the entire line profile should be shifted). Weak ($\leq 50 \text{ km s}^{-1}$) blue-shifts in Fe XIV and Fe XVI lines were also found, while lower-temperature lines showed red-shifted profiles.

The other flare, which is discussed here, occurred on 2007 May 22. It was a much weaker flare, of class B2, however for many reasons small flares are sometimes much better targets for an instrument such as EIS. For example, compact flares can be observed within the field-of-view of EIS. Also, large flares can produce very intense, broad and shifted lines, which provide added complexities in the analysis.

2. Data and observations

The flare occurred in the active region AR 10956 on 2007 May 22. It was observed in soft X-rays with GOES and *Hinode*'s X-Ray Telescope (XRT), in the extreme-ultraviolet (EUV) with the Transition Region and Coronal Explorer (TRACE) and *Hinode* EIS; the optical range was covered by *Hinode*'s Solar Optical Telescope (SOT), as well as TRACE white-light and Big Bear magnetograms. Unfortunately, the flare was not observed by RHESSI (hard X-rays). However, the flare was recorded at radio wavelengths with the Nobeyama Radioheliograph (NoRH). Apart from EIS, which is described further below, the data were reduced with the standard Solarsoft¹ analysis programmes.

Figure 2 shows an XRT image of the location of the flare on the solar disk (NW region), with the TRACE field-of-view

¹ http://www.lmsal.com/solarsoft/ssw_whatitis.html

XRT 23:19:37 UT Open+Ti-Poly

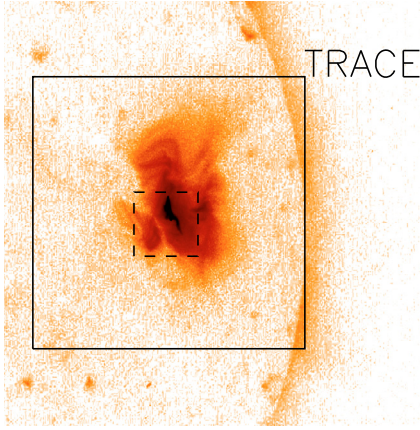


Fig. 2. *Hinode*/XRT (negative) image, with the field-of-view of the TRACE observations (larger box), and a smaller window ($2' \times 2'$) used for *Hinode*/SOT, *Hinode*/XRT and TRACE (see figures below) chosen to show the details of the evolution of the flare.

(large box) and the selected smaller region which was chosen to study the evolution of the flare. Note that both the XRT as well as TRACE field-of-view contain part of the solar limb. This was used to co-align images. *Hinode*'s XRT used the Ti/Poly filter at the time of this observation (Kano et al. 2008). There are a few exposures containing a large part of the Sun, including the right limb, and others with a smaller field-of-view over the flare region. It also observed the whole Sun in visible light (G-band) at 4305 Å. We used the XRT/G-band (and XRT limb fitting) to obtain the pointing of the XRT images and also to estimate the co-alignment of SOT/FG data. The XRT pointing needed to be corrected for satellite jitter. The X-ray exposures of the enlarged flare region were taken at a 20 s cadence for 3 min, another exposure after 1 min, then a 6 min break and repeating this cycle several times. The data is saturated where the flare emission is strongest.

TRACE observed the AR with a sequence of 171 Å band images and occasionally at 1600 Å. The pointing was checked by looking at the location of the solar limb, which is caught in the top right hand corner of the TRACE field-of-view (see Fig. 2), and by co-aligning the white-light images with SOT/FG.

Full-disk magnetograms from the Big Bear Solar Observatory are available at 10 min intervals and were mainly used to co-align *Hinode*/SOT data. *Hinode*'s SOT comes in two configurations, spectro-polarimeter (SP) and filtergrams (FG) (Tsuneta et al. 2008). SOT/SP observed the flare region at 22:47 UT. Thereafter and during the flare, SOT observed in FG mode at the usual 1 min cadence, rotating filters between the green continuum (555.05 nm), the blue continuum (450.45 nm) and the chromospheric line Ca II H (396.85 nm), with a bandwidth of 0.4 nm (green and blue) and 0.3 nm (Ca II H), respectively.

The Nobeyama Radioheliograph (NoRH; Nakajima et al. 1994) observes the Sun every day from 22:45 UT for around 8 hours at 17 GHz at a spatial resolution (beamsize) of 10 arcsec and a pointing accuracy of about 5 arcsec at best. For the duration of the flare, the radio data was processed with the “fujiki” routine (Fujiki 1997). We obtain data at a cadence of 10 s. Note that this event did not trigger flare mode for the radio observation nor was it cataloged as a NoRH flare. Co-aligning radio images with all the above data gives a shift of (6, −7) arcsec. Note,

Table 1. Starting and ending times (UT, hh:mm:ss) for the EIS “CAM_ARTB_RHESSI_b_2” rasters on 2007 May 22 discussed here.

No.	Start	End
1	22:57:25	23:01:15
2	23:01:17	23:05:07
3	23:05:10	23:09:00
4	23:09:03	23:12:53
5	23:12:55	23:16:45
6	23:16:48	23:20:38
7	23:20:41	23:24:31
8	23:24:34	23:28:24
9	23:28:26	23:32:16
10	23:32:19	23:36:09

Table 2. A selection of lines we included in the “CAM_ARTB_RHESSI_b_2” EIS study.

Ion	Wavelength (Å)	Log T_m^* (K)	Note
He II (bl)	256.32	–	EIS core line
O V (bl, sbl)	192.91	5.5	
O V	248.49	5.5	
O VI	184.12	5.5	
Mg V	276.581	5.5	
Mg VI	268.991	5.6	
Fe VIII (bl)	185.21	5.6	
Mg VII	278.39 (bl Si VII), 280.75	5.8	Ne (10^9 – 10^{11})
Fe XII (sbl)	195.12	6.1	EIS core line
Si X	258.37, 261.0	6.1	Ne (10^7 – 10^{10})
Fe XIII	202.0, 203.8	6.2	Ne (10^9 – 10^{11})
Fe XIV	264.79, 274.2 ^{EM} (bl)	6.2	Ne ($10^{8.5}$ – 10^{11})
Fe XV (bl)	284.16	6.3	
Fe XVI	262.98 ^{EM}	6.4	
Fe XVII	269.41 ^{EM}	6.6	
Ca XVII (bl)	192.82 ^{EM}	6.7	EIS core line
Fe XXIII (bl)	263.76 ^{EM}	7.1	
Fe XXIV (bl)	192.03 ^{EM}	7.1	

Notes. (*) Approximate temperature of peak abundance in ionisation equilibrium. Line ratios used for density measurements are indicated with Ne, with their range of sensitivity (in cm^{-3}). bl and sbl indicate blending and self-blending, respectively. (^{EM}) lines used for the emission measure plots (Fig. 14).

however, that the spatial resolution of the radio data is too large to distinguish with what other emission (i.e. Ca II H or X-ray) it correlates best, other than that it originates from the same event. We also analysed the polarised 17 GHz data but found that the rate of polarisation is below 1% and therefore negligible.

2.1. EIS observations

The *Hinode*/EIS CAM_ARTB_RHESSI sequence consists of a context raster ($240'' \times 240''$) which lasts ~ 20 min, followed by a series of $40'' \times 120''$ high-cadence rasters (CAM_ARTB_RHESSI_b_2), lasting about 4 min each, in which the EIS slit rasters (from west to east) with 20 exposures and 10 s exposure time. In contrast to many other EIS observations, carried out with the 1'' slit, we chose to use the 2'' slit, which gives twice the counts without losing any spectral or spatial information. Indeed, the spectral resolution in the 1'' and 2'' spectra is similar, and the spatial resolution of EIS exceeds 2''. Table 1 lists the times of the EIS rasters which cover the flare.

We designed the EIS observing sequence to have high-cadence but also cover a wide range of temperatures. Figure 1 shows the contribution functions of some of the lines used in this analysis. Also, we included line pairs formed at both transition region and coronal temperatures with density diagnostics capability from Mg VII, Si X, Fe XII, Fe XIII and Fe XIV. Table 2 lists some of the main lines included in the sequence. The total number of lines is about 50. This EIS sequence was designed to be run over on-disk active regions, when possible in coordination with complementary instruments (XRT and SOT on board *Hinode*, RHESSI, TRACE, SOHO/CDS).

As described in Del Zanna (2008a), the analysis of EIS data needs to take into account the strong (75 km s^{-1}) orbital variation of the wavelength scale during the 90 min orbit and the offsets in both N-S ($18''$) and E-W ($2''$) directions between the two channels. The offset in the E-W direction means that observations in the two channels were not simultaneous or co-spatial (The E-W offset was partly corrected for in late 2008). During the course of benchmarking Fe XVII (Del Zanna & Ishikawa 2009), it was also found that the spectra are slanted relative to the axes of the CCD by $3.66(\pm 0.2)$ pixels end-to-end (each pixel along the slit corresponds to $1''$). A small tilt is also present. The wavelengths were obtained by applying an orbital correction based on the wavelengths of the few strongest lines, measured in the bottom part of the EIS field-of-view.

Another problem with the EIS observations is the jitter of the field-of-view. There are at least two types of jitter, caused by thermal cycles along the 90 m orbit of *Hinode*. One is a spacecraft jitter, of the order of few arc sec and with short timescales. Another one is an internal EIS jitter, which is also present. The net effect is that the EIS FOV jitters quite randomly by about $3\text{--}4''$ with time-scales of the order of a few minutes. The TRACE 171 \AA images were used to find the pointing of each of the EIS rasters, by cross-correlating the TRACE images with monochromatic EIS images in Fe VIII. The *cfit* package (Haugan 1997) was used to fit Gaussian profiles to all the lines observed, with a few exceptions, described below.

3. Evolution of the flare

3.1. Context observations

Figure 3 (top) shows both GOES light curves (green: $1\text{--}8 \text{ \AA}$, blue: $0.5\text{--}4 \text{ \AA}$) of the flare on a logarithmic scale. Pre-flare emission begins shortly after 23:00 UT, while the main phase of the B2-class flare starts around 23:18 UT, peaks at about 23:26 UT, and is over by 23:45 UT. The horizontal arrows (GOES BG) indicate a quiet time interval which is used as background emission to later determine the temperature based on the two GOES channels, while the vertical dotted lines and the numbers designate the timings of the EIS rasters. Figure 3 (lower panel) shows a zoom-in of the flare light curve. The green line is the soft GOES channel ($1\text{--}8 \text{ \AA}$), while the blue line is the harder channel ($0.5\text{--}4 \text{ \AA}$). The respective background is indicated by the dotted line. The bottom plot shows the isothermal temperature (red line) obtained from the GOES light curves. A peak temperature of about 10 MK is obtained. Note that GOES observes the full Sun in two broad spectral ranges, dominated by continuum emission as well as many emission lines formed over a broad temperature range. The temperature can only be reliably calculated for the times where both GOES light curves have emission above their backgrounds (White et al. 2005).

The flare occurred in an active region which was relatively active in previous days (Chifor et al. 2008; Sterling et al. 2010)

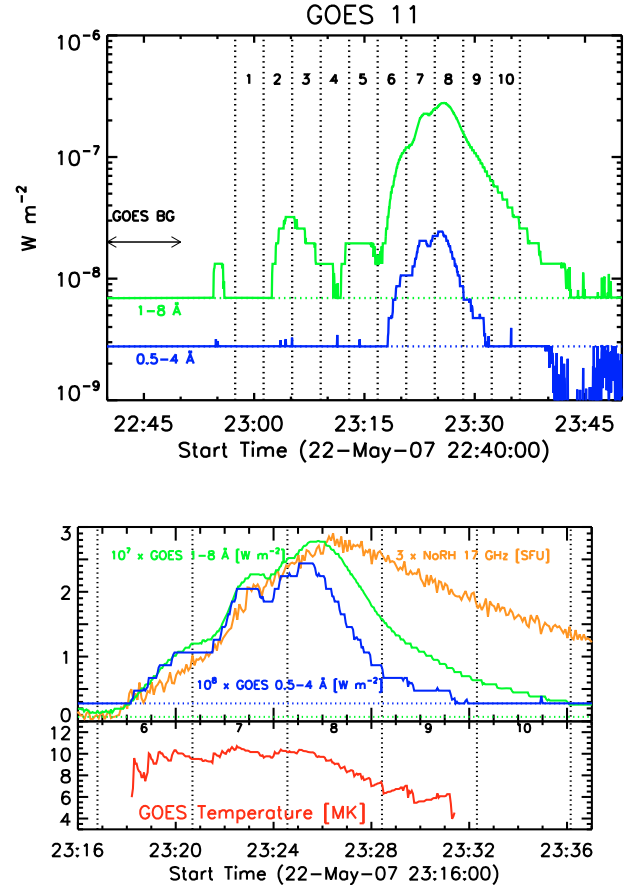


Fig. 3. Top: GOES light curves (in two channels) of the 2007 May 22 flare. Shown on the left is the region chosen for background subtraction (GOES BG). The timings of the 10 *Hinode*/EIS rasters discussed in this paper are indicated with vertical dashed lines and numbered (see Table 1). Middle: a zoom-up of the GOES light curve, with superimposed the NoRH 17 GHz emission. Bottom: the isothermal temperature obtained from the GOES light curves.

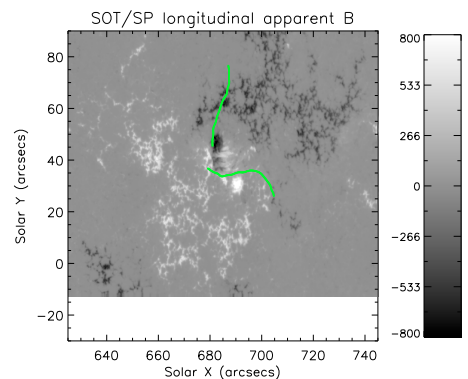


Fig. 4. The apparent longitudinal magnetic field (Gauss) from *Hinode*/SOT SP data. The location of the two ribbons as identified in the SOT Ca II H data (Fig. 5) is displayed by the green line.

and located in the NW region, as shown in Fig. 2. The AR was mainly composed of two opposite-polarity regions with two sunspots (see Fig. 4). Strong longitudinal and transverse magnetic fields were present in a region close to the northern Sunspot, where the flare occurred.

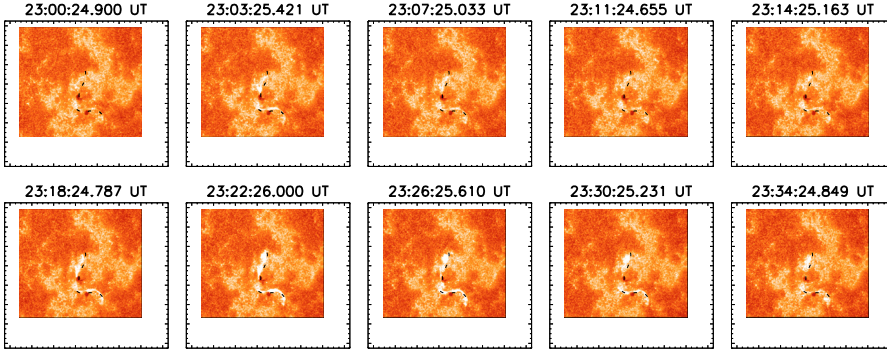


Fig. 5. *Hinode*/SOT Ca II H broad-band images during the times of the *Hinode*/EIS observations. The location of the two ribbons is highlighted. The field of view is $2' \times 2'$.

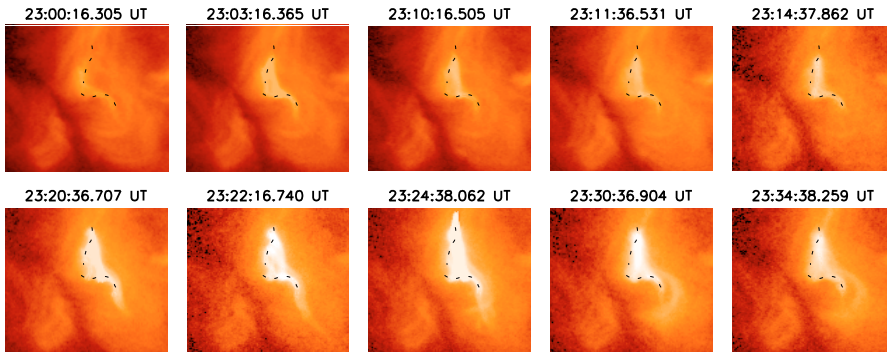


Fig. 6. *Hinode*/XRT images close to the times of the *Hinode*/EIS observations. The location of the two ribbons is shown. The field of view is $2' \times 2'$.

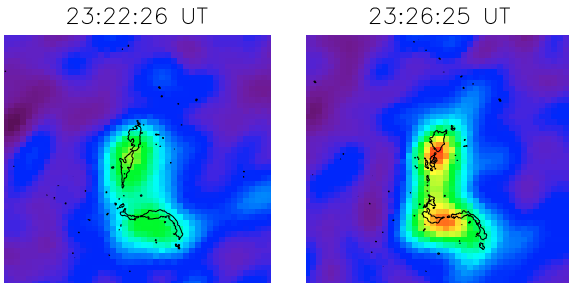


Fig. 7. NoRH images at 17 GHz during the EIS flare rasters Nos. 7 and 8, respectively, with superimposed contours of the SOT/Ca II H emission. The field of view is $110'' \times 110''$.

Figures 5 and 6 show the evolution of the flare as observed in Ca II H by *Hinode*/SOT and in soft X-rays by *Hinode*/XRT. The images corresponding to the times of the 10 EIS rasters analysed here are shown in the figure. The Ca II H images clearly show the brightening of two ribbon structures (highlighted by the dashed line), located in the opposite magnetic polarities (cf. Fig. 4). The *Hinode*/XRT images in Fig. 6 show strong enhancements nearly co-temporal with the Ca II H brightenings in the ribbon and in the region in between them. An exact comparison is not possible due to the low cadence of the XRT data, compared to SOT.

The NoRH 17 GHz flux in SFU (solar flux unit) is shown in Fig. 3. The pre-flare flux was subtracted so the light curve shows only the flare component. The intensity is very weak for a radio flare. Even so, the gradual evolution of the radio flux, which is similar to the GOES profiles, suggests that they are from thermal origin. Figure 7 shows two radio images at 17 GHz overplotted with the SOT Ca II H emission. Note that the spatial resolution and pointing uncertainty of the 17 GHz emission is so large that it is hard to relate this emission with what is seen at other wavelengths. Nevertheless, the 17 GHz emission appears to be only nearly co-spatial with the ribbons as seen in Ca II H and reaches

its peak emission in raster No. 8 only (around 23:26 UT), as does the X-ray emission, as opposed to the Ca II H emission, which is already at its brightest emission during raster No. 7 (around 23:22 UT). From the absence of polarised emission we can exclude gyro-resonant emission caused by strong magnetic fields, and identify a likely cause for the bulk of the 17 GHz emission being thermal plasma at around 1 MK (cf. Hanaoka 1999).

The TRACE 171 Å images indicate that the majority of coronal structures at 1 MK are not affected at all by the flare. However, a closer inspection obtained by looking at base-difference images (Fig. 8) shows that at the same time as the ribbons brightened an eruption of what is presumably filament material originated from the southern ribbon, and was ejected after 23:20 UT towards the SW of the field-of-view.

3.2. EIS observations

Figure 9 shows a selection of results obtained from the 10 EIS rasters. The intensities of chromospheric (e.g. He II) and middle-TR lines (e.g. O V, Mg V, O VI) show strong enhancements in the two ribbons just before and during the peak phase (cf. O VI in Fig. 9), consistent with the *Hinode* SOT Ca II H broad-band images. Coronal lines formed between 0.8 and 1.5 MK do not show any appreciable changes (in terms of spectral line profiles and intensities) throughout the flare, as Fe XII in Fig. 9 shows. In the early EIS rasters, before 23:18 UT, there is no measurable emission in the flare ($T > 10$ MK) lines of Fe XXIII and Fe XXIV. The first indication of high temperature emission, around 10 MK, occurs during raster No. 7 (see Fig. 9). A brightening and a high-temperature loop structure was observed in this raster, during 23:20–23:22 UT. It connected two regions in the ribbons where strong blue-shifts were observed in Fe XIV–Fe XVI lines, as shown in the fourth and fifth row of Fig. 9. The fourth row shows the Doppler map of the centroid of the main component of the Fe XVI 262.984 Å line. The fifth row shows the intensities

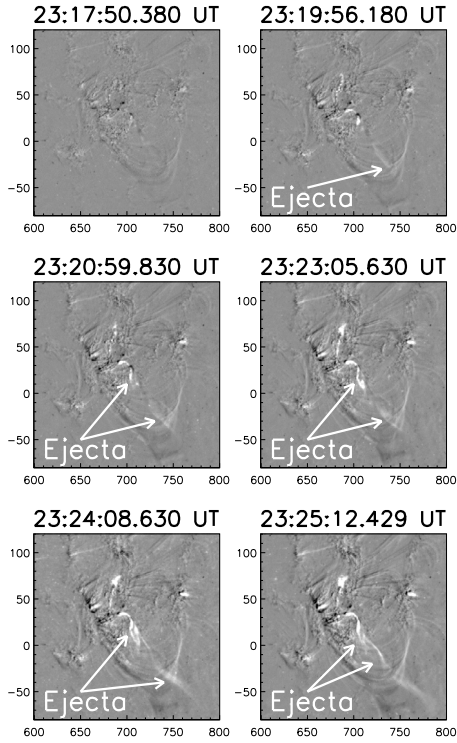


Fig. 8. TRACE 171 Å base-difference images showing the eruption of filament material from the flare region towards the SW (*bottom right*). Units are arcseconds (abscissae along the E-W and ordinates along the N-S direction) from Sun centre.

of the blue-wing (bw) component of the same line (see below for a discussion on line profiles).

Another, much stronger high-temperature loop structure was observed in the following raster No. 8, between 23:25 and 23:26 UT in Fe XXIII and Fe XXIV. Again, strong blue-shifts were observed at the footpoints of this structure, in Fe XIV–Fe XVI lines. This is clearer in Fig. 10 where a zoom of the flare region is shown. The geometry in this case is particularly favourable for EIS, since the loop was aligned N-S along the EIS slit, hence the loop and its footpoints were observed almost simultaneously.

It is clear that the regions with stronger blue-shifts are located on the ribbons and at the footpoint locations of the 6 and 10 MK loops seen in Fe XVII and Fe XXIII. The intensities in lines formed over 3–4 MK are enhanced at the footpoint locations, which is indicative of very high densities (as discussed below and measured from the Fe XIV line ratio). The Fe XVII intensity is also enhanced at the footpoints. It is very likely that this is the same feature observed with the Skylab S-054 X-ray telescope at 2'' resolution by Kahler et al. (1975), and termed “X-ray kernels”. These authors studied C-class flares and found that very bright kernels developed during the impulsive phase, at the footpoint locations of loops (often unresolved) that later formed and connected them. Indeed, the S-054 X-ray filters were dominated by Fe XVII or ions formed at similar temperatures.

We note that the evaporation, marked by the blue-shifts in Fe XIV–Fe XVI lines, starts before the peak emission of the high-temperature plasma, as it is clearly present during rasters Nos. 5 and 6 (see below for a discussion on a kernel). Some pre-flare evaporation also seems to take place in EIS rasters Nos. 2 and 3 during the pre-flare emission (see the GOES light curve of Fig. 3). The absence of hot (10 MK) flare plasma suggests that

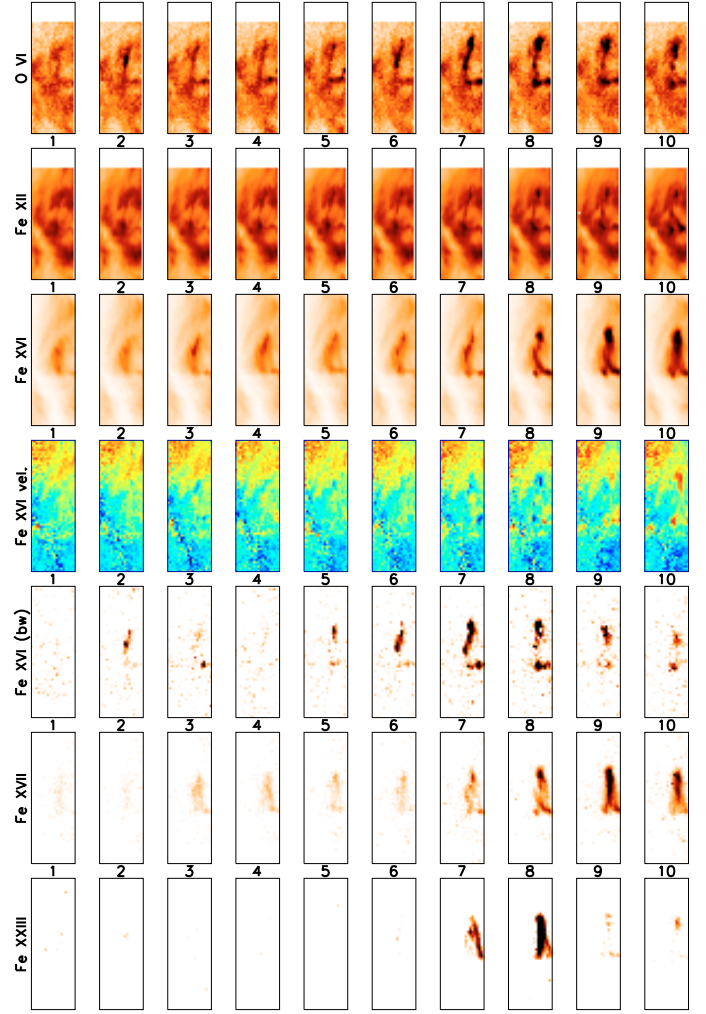


Fig. 9. Monochromatic (negative) images from the 10 *Hinode* EIS rasters in a selection of lines. *From top to bottom:* O VI 184.1 Å, Fe XII 195.11 Å, Fe XVI 263 Å intensities; Doppler image of the centroid position of the Fe XVI line; intensity of the blue-wing (bw) of the Fe XVI line; intensity in Fe XVII 269.41 Å and Fe XXIII 263.7 Å. The field of view is 40'' × 120''.

thermal conduction is not the cause of these pre-flare blue-shifts, although it is possible that densities during this early phase are so low that line intensities are below the sensitivity limit of the instrument. An X-ray spectrometer might be needed to resolve this issue.

The high-temperature main loop structure disappeared quickly and was not observed during the following raster No. 9 over the same area, at 23:29–23:30 UT. Interestingly, during the following raster No. 10, strong red-shifts are observed in the same footpoint regions where the blue-shifts were previously present. This is indicative of cooling plasma flowing back down towards the chromosphere, as expected from theory.

As soon as the Fe XXIII and Fe XXIV emission disappears, strong enhancements in lines formed around 6 MK (Fe XVII, Ca XVII) are observed in the loop. The peak emission in these lines was observed during the raster No. 9, between 23:28 and 23:30 UT. The cooler Fe XVI emission appears to peak in the following raster, No. 10, when the loop was observed at 23:32–23:34 UT. Unfortunately, this was the last raster of the sequence so we could not follow the cooling any further. We can rule out

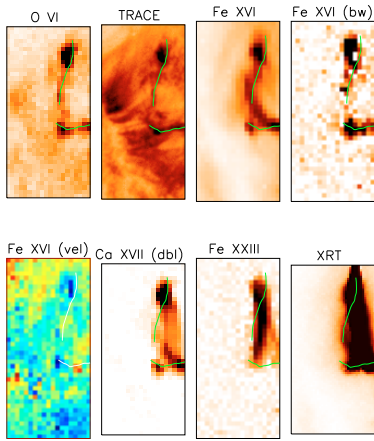


Fig. 10. Results from the EIS raster No. 8, 23:24–23:28 UT. *From the top left:* intensity of O VI 184.1 Å; intensity of TRACE 171 Å; intensities of the main and blue-wing components of the Fe XVI 263 Å line; Doppler image of the centroid position of the main Fe XVI line; intensity in the Ca XVII, de-blended; intensity in Fe XXIII 263.7 Å; intensity in XRT (partly saturated). The TRACE 171 Å image was taken at 23:26:15 UT, while the XRT one at 23:24:38 UT. Superimposed is the location of the ribbons. Note that there is a slight offset in the vertical between the two EIS channels which has been accounted for. The field of view is $40'' \times 80''$.

that the peak emission in Fe XVI occurred before 23:30, but we cannot rule out that it could have occurred after 23:34 UT.

3.3. A discussion about line blending with EIS

The strong He II 256.32 Å line is blended with a host of strong transitions. A preliminary discussion was given in [Young et al. \(2007\)](#). A more in-depth analysis indicates that this line is blended with Si X, Fe XII, Fe XIII, Fe X, and some unidentified coronal emission. Its use is therefore very challenging. Proper de-blending can be done only if many other lines are observed. Even for this case, only intensities can be derived reliably, it is not possible to study line profiles. The Si X 256.3 Å contribution can be removed easily when the 261 Å line is observed because these lines form a branching ratio and hence their ratio is well known. The contribution from Fe XIII is not easy to remove because the blended line is strongly density-dependent, hence accurate density measurements from other unblended Fe XIII lines are required. Here, we used the 202.0 and 203.8 Å lines to derive electron densities (though the second is blended). Contributions from Fe XII and Fe X (see [Del Zanna & Mason 2005](#); and [Del Zanna et al. 2004](#)) are also complex to estimate because the lines are density-sensitive. Figure 11 (top row) shows the results for the He II 256.32 Å line deblended of Si X and Fe XIII for one EIS raster, and a low temperature transition region line (Mg V 276.581 Å) for comparison, showing that the ribbons are clearly delineated.

The strong O V 192.91 Å line is actually a self-blend of a number of transitions. In most EIS active region and flare spectra, it becomes severely blended with Fe XI and Ca XVII (see Fig. 12).

We included the weaker O V 248.49 Å line in the EIS study so we could estimate (still with some uncertainty) the intensity of the O V transitions at 192.91 Å.

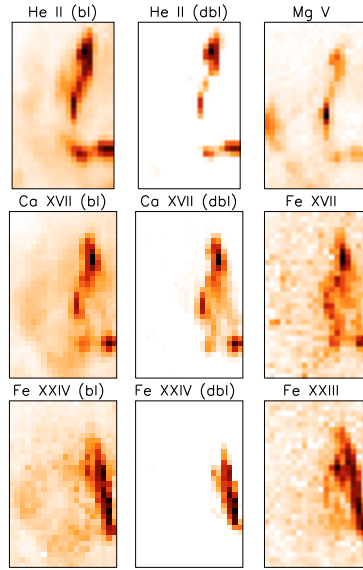


Fig. 11. *Top:* EIS images in the blended He II 256.3 Å, deblended He II, and Mg V 276.581 Å. *Middle:* EIS images in the Ca XVII 192.82 Å (blended and de-blended) and Fe XVII 269.4 Å. *Bottom:* EIS images in the Fe XXIV 192.03 Å (blended and de-blended) and Fe XXIII 263.76 Å. These examples were taken from raster No. 7. The field of view is 40'' × 60''.

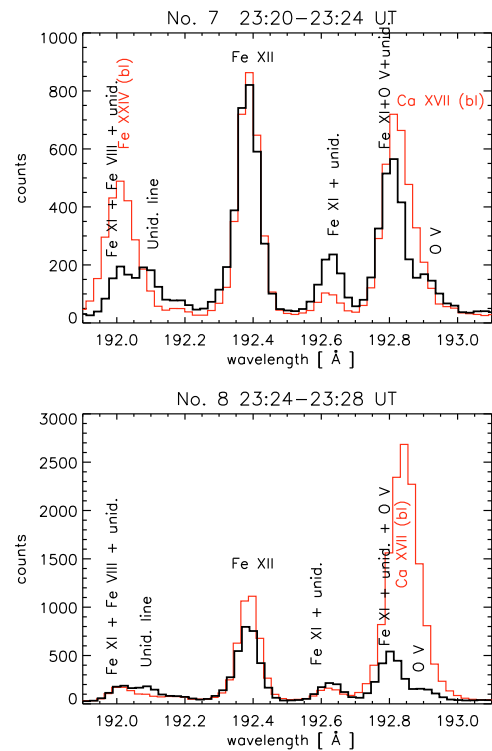


Fig. 12. The EIS spectral window containing the flare lines Fe xxiv and Ca xvii. *The top and bottom spectra* (thin red lines) are taken during the two flare rasters Nos. 6 and 7. Reference spectra are taken from an area outside the flare region, and are shown in thick black. Note the presence of various blends.

The strong Mg VII 278.39 Å line is useful for density-diagnostics, but is severely blended with a Si VII transition. Fortunately, this latter transition is a branching ratio with the Si VII 275.383 Å line, so the Mg VII 278.39 Å line can be deblended quite accurately. The Fe XII 195.12 Å line is a self-blend of two transitions identified in [Del Zanna & Mason \(2005\)](#), although the weaker transition only blends significantly with the stronger one in its red wing when electron densities are very high, well above 10^{10} cm^{-3} .

The Fe XIV 264.79 Å line is largely free of blends in active region spectra, although a recently-identified Fe XI line is present (Del Zanna 2010) but weak. The Fe XIV 274.20 Å line is blended with a Si VII 274.175 Å line. The contribution of the Si VII line can be estimated from the intensities of other Si VII lines, for example the Si VII 275.383 Å line.

The strong Fe XV 284.16 Å line is blended with a strong Al IX and a newly-identified Fe XVII line (Del Zanna & Ishikawa 2009). The strong Fe XVI 262.984 Å line is largely free of blends in active region spectra, although some unidentified transition region emission seems to be present (Del Zanna 2009a).

The Ca XVII 192.82 Å resonance line (see Fig. 12) is a complex blend studied by several authors (e.g., Young et al. 2007; Ko et al. 2009; O'Dwyer et al. 2010). Recently, Del Zanna (2009a) has analysed in detail O V lines, confirming that, when no coronal emission is present, good agreement between predicted and observed O V lines is found. Hence, no further transition region lines appear to blend this line. Also recently, Del Zanna (2010) discusses new atomic data and line identifications for Fe XI, and confirms that, although the Fe XI is dominant, some contribution due to an unknown coronal line is present.

During flares, the O V lines can become bright and broad, and it therefore becomes virtually impossible to obtain any reliable Ca XVII Doppler or line width measurement. Deblending can be done though, in the sense that the Ca XVII 192.82 Å emission can be estimated. We have used the observed O V 248.49 Å line intensity to estimate the O V contribution, although the lines are density-sensitive so a large uncertainty is present. The strong Fe XI 192.813 Å line forms a branching ratio with the 188.216 Å line (Del Zanna et al. 2010; Del Zanna 2010) so it is straightforward to estimate the Fe XI contribution to the Ca XVII 192.82 Å resonance line. Figure 11 (middle row) shows the results of Ca XVII deblending for one particular EIS raster. The Fe XVII 269.4 Å line is given for comparison with the Ca XVII deblended line. The same morphology is seen, as expected, given that the two ions are formed at similar temperatures.

As discussed in Del Zanna & Ishikawa (2009), the Fe XXIII 263.76 Å line is clearly blended with emission which is always present in the EIS active region spectra and has a morphology very similar to Fe XII (cf. Fig. 1 in that paper). This emission should be considered still unidentified, although laboratory measurements have indicated the presence of Fe XIV (Churilov & Levashov 1993) and Fe XV (e.g. Redfors 1988) lines at these wavelengths. However, the current CHIANTI v6 atomic data for Fe XIV and Fe XV indicate that these laboratory lines are very weak, i.e. not observable in solar spectra. The lines are actually very close in wavelength, at 263.65 Å and 263.70 Å, as shown in Fig. 13 (bottom), from a spectrum obtained from the 2007 May 21 observations discussed in Del Zanna & Ishikawa (2009). This observation had a long (90 s) exposure, which is needed to clearly measure these weak lines.

During the benchmark of Fe XXIII (Del Zanna et al. 2005), it was found that the best wavelength measurement for the intercombination line was 263.765 Å, i.e. close but still resolvable from the two unidentified lines. A further weak blend is present in the red wing of Fe XXIII. We therefore conclude that any measurement of profile asymmetries for Fe XXIII is very difficult, until a clear understanding of the blends is achieved.

The Fe XXIV 192.03 Å line is blended with several other lines: an unidentified TR line (Del Zanna 2009a), a line from Fe VIII (Del Zanna 2009b) and a line from Fe XI (Del Zanna 2010) at least. In active region spectra, the dominant blend

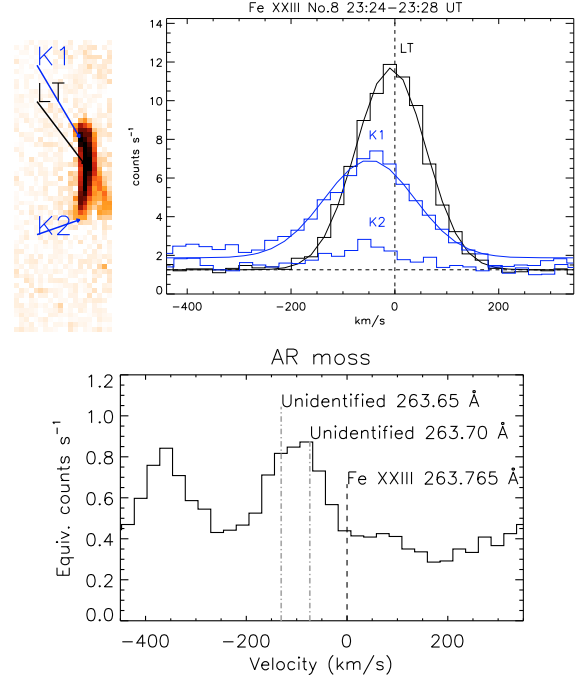


Fig. 13. Top left: image in the Fe XXIII 263.765 Å line during the flare raster No. 8, showing the selected locations of the Loop Top (LT) and the two footpoint regions, (kernels K1 and K2). The field of view is $40'' \times 120''$. Top right: the EIS spectral window containing the Fe XXIII 263.765 Å line during the flare raster No. 8. The thick black spectrum refers to the area of peak emission at the Loop Top (LT), where the line profile is symmetric and at rest wavelength. The spectra in blue are taken from the two footpoint regions, (kernels K1 and K2), and show slightly broadened and blue-shifted line profiles. The bottom figure shows an active region spectrum obtained on 2007 May 21 with the $1''$ slit where the presence of two unidentified coronal lines in the blue-wing of Fe XXIII is highlighted. The spectrum is in equivalent count rates, for a direct comparison.

comes from the Fe XI 192.021 Å line, which fortunately forms a branching ratio with the 201.734 Å line, which was included in the EIS study discussed in this paper. Figure 11 (bottom row) shows the results of Fe XXIV (deblended of Fe XI) for one of the rasters. The Fe XXIII 263.765 Å emission is given for comparison, and shows very similar features.

In conclusion, it is possible to reconstruct the line intensities for He II, Ca XVII and Fe XXIV by taking account of the various blends. However, it is virtually impossible, at least for small flares, to obtain reliable Doppler or line width measurements for these lines from EIS spectra.

3.4. Flare loop top: EM, temperature and electron densities

The intensity $I(\lambda)$ of a spectral line is normally expressed as:

$$I(\lambda) = \int_{\text{h}} N_e N_H A(X) G(N_e, T, \lambda) dh \quad (1)$$

where $G(N_e, T, \lambda)$ is the contribution function of the line, N_e, N_H are the electron and hydrogen number densities, $A(X)$ is the element abundance (relative to hydrogen), and the integral is along the line-of-sight h . The column emission measure is defined as $EM_h = \int_{\text{h}} N_e N_H dh$. If the plasma is isothermal (say $T = T_0$), $EM_h = I / (A(X) G(N_e, T_0))$. Hence, the loci of the $I / (A(X) G(N_e, T_0))$ curves represent the upper limits to the

emission measure (see, e.g., Del Zanna et al. 2002b). We have produced emission measure (EM) loci plots for various regions at various times during the flare. The emission measure plots allow an estimate of the electron temperatures and densities during the flare assuming ionisation equilibrium. They were obtained with atomic data from v.6 of the CHIANTI package (Dere et al. 2009), the latest recommended “photospheric” chemical abundances from Asplund et al. (2009), and the new CHIANTI v.6 ion abundances. We would like to point out that the main uncertainty in the EM_h estimate is the absolute radiometric calibration of the EIS spectrometer, and the elemental abundances. If, for example, “coronal” abundances were used, and the iron and calcium abundances increased by a factor of three, then the EM_h would be lower by the same amount.

In order to isolate the flare loop contribution from the foreground/background emission, we have subtracted pre-flare intensities (from raster No. 4) at the same locations. The EM loci curves for the hot loop top location during the last three EIS rasters, Nos. 8, 9, 10, are shown in Fig. 14.

Let us consider the first plot for raster No. 8, 23:24–23:28 UT, when peak flare emission occurs. The EM curves for Fe XVI, Fe XVII, Fe XXIII and Fe XXIV are consistent with a flaring loop being isothermal at a temperature of about 10 MK. This is a very reasonable value for a B-class flare, and is in excellent agreement with the temperature obtained from the ratios of the GOES fluxes (Fig. 3), and with the accurate temperatures at flare maximum of similar-class flares obtained by Feldman et al. (1996) using the satellite lines observed with the Bragg crystal spectrometer (BCS) on-board Yohkoh.

If one assumes that the plasma is uniformly distributed along the line-of-sight, $EM_h \approx 0.83 < N_e >^2 \Delta h$, where Δh is the depth of the emission layer (we have assumed $N_H = 0.83N_e$ considering a fully ionized gas with the relative helium abundance $A(\text{He}) = 0.1$). If the depth of the emission layer is known, from the emission measure it is possible to estimate $\langle N_e \rangle$. If the plasma is not uniformly distributed, but for example is composed of a clump of high-density region surrounded by vacuum, then the so-called *spectroscopic filling factor* would be less than one, and the derived $\langle N_e \rangle$ would represent a lower limit to the real density. Conversely, if an averaged density is known from e.g. a line ratio, it is then possible from the emission measure EM to estimate the depth of the emission layer. The width of the loop structure as seen in the hottest Fe XVII, Fe XXIII and Fe XXIV lines is about 2–4″. The emission measure at 10 MK provides corresponding densities $\langle N_e \rangle$ of about $4\text{--}6 \times 10^{10} \text{ cm}^{-3}$.

Four minutes later, at 23:28–23:32 UT, no significant Fe XXIII or Fe XXIV emission was present (upper limits for Fe XXIII emission are shown in Fig. 14 for rasters Nos. 9 and 10). The plasma temperature has dropped to about 6 MK, and the emission measure indicates densities of about $3\text{--}5 \times 10^{10} \text{ cm}^{-3}$. After another 4 min, during the EIS raster No. 10 (23:32–23:36 UT), the temperature has further dropped to 4.5 MK, as can be seen in Fig. 14 (bottom panel). These changes in the EM Loci curves clearly show how the flare loop is cooling.

3.5. Flare kernels: source regions of chromospheric evaporation

We examined the profiles of all the lines in the different locations, and found that only lines from Fe XIV, Fe XV and Fe XVI which are formed in a narrow temperature range (2–3 MK) showed strong asymmetries, with a blue-wing enhancement in kernels located on the ribbons and at the footpoint location of the hot 10 MK loops.

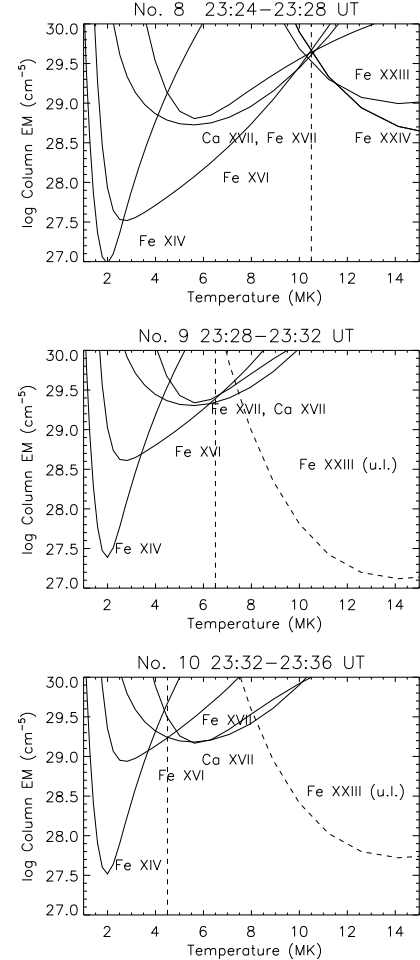


Fig. 14. The EM Loci figures for the flare loop top region during the last three EIS rasters, Nos. 8, 9, 10. The lines displayed are listed in Table 2. In the two lower panels, the Fe XXIII curve is based on an upper limit (u.l.) on the intensity of the line.

The line widths in the EIS spectrometer are mostly instrumental. In the LW channel, of particular interest here, the instrumental width increases linearly with the position along the slit (details will be published elsewhere). In the central part, where the observations were taken, the full-width-at-half-maximum ($FWHM$) for the LW lines is about 75 mÅ in the quiet Sun. In active regions, most lines have a $FWHM$ of 80 mÅ, with the exception of the very strong Fe xv 284 Å line, which has a width of 90 mÅ. In most locations, line profiles are very symmetric.

Figure 15 shows two sample profiles from the strong Fe XVI 263 Å line, obtained during the “pre-flare” raster No. 6 (well before the 10 MK emission appears). The black profile is from a foreground (FG) location in the core of the active region. As in all locations of the rasters (with the exception of the kernel regions), the line profile is very symmetric and centred at the rest wavelength (a region in the southern field-of-view was chosen to measure rest wavelengths). The blue, highly asymmetric profile is from a kernel (K) region just a few arc-seconds north. The blue-wing asymmetry extends to velocities larger than 200 km s⁻¹, and can be fitted with multiple components. Since we are interested in obtaining an estimate of the overall intensity of this secondary component, we fitted the line profile with two Gaussians, the main one at the rest wavelength (with fixed $FWHM = 80$ mÅ), and a secondary one. The intensity

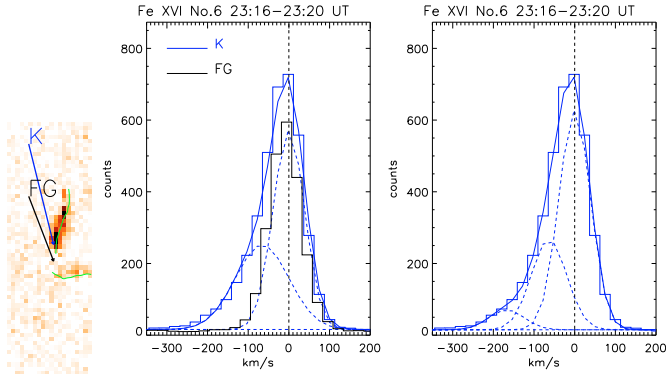


Fig. 15. *Left:* image of the intensity of the blue-wing component in Fe XVI (recorded by EIS during the scan No. 6; the field of view is $40'' \times 120''$) with two selected regions, a foreground (FG) location in the core of the active region, and kernel (K) region just a few arcseconds north, in the northern ribbon. *Middle:* profiles of the Fe XVI 263 Å line, in the two regions. The dashed vertical line indicates the rest velocity, while the dashed lines are the Gaussian profiles of the main and secondary components of the spectrum in the kernel (K). *Right:* the same spectrum in the K region, fitted with three Gaussian components.

of the main component (dashed line) turns out to be close to the foreground one, as shown in Fig. 15 (middle). This is as expected, since we believe that the rest component originates from the foreground active region plasma. We interpret the secondary, blue-wing component as arising solely from the kernel region, source of the chromospheric evaporation. The intensity, Doppler velocity and width of this component are considerable (see Table 3). An alternative is to consider multiple secondary components having similar widths as the instrumental one. With two such components (bw1 and bw2, see right plot in Fig. 15 and Table 3) a good fit is obtained. The two components have remarkable line-of-sight velocities, about 60 and 170 km s⁻¹.

All the strong, un-blended lines formed at similar temperatures (in particular the Fe XIV 264.787, 274.203 Å lines) show similar characteristics, and were fitted with a two-component Gaussian profile. The strong Fe XV 284.16 Å line does show the same features, but it is blended in its blue-wing with Al IX and a recently-identified strong Fe XVII line (Del Zanna & Ishikawa 2009) which complicates the measurement.

We can rule out the presence of blue-wing enhancements in lower-temperature lines, because the line profiles of the very strong Fe XIII, Fe XII, Fe XI, Fe X, Fe VIII emission lines show no asymmetries. On the other hand, we cannot rule out the presence of some asymmetry in the hotter lines, because they are either weak or blended.

Coronal line profiles with persistent shifts towards the blue or with persistent blue-wing asymmetries have been routinely observed by EIS in active region spectra (see, e.g. Del Zanna 2008b; Doschek et al. 2008; Hara et al. 2008; Peter 2010). They are often referred to as “coronal outflows”. We would like to point out that the blue-wing asymmetries observed here are very different, for a number of reasons. First, they are very localised at the footpoint of flare loops, contrary to the coronal outflows, which are also very localised (on plage/Sunspot regions), but then have a very rapid spatial expansion at greater heights (Del Zanna 2008b). Second, they are not observed in Fe XIII, Fe XII lines, contrary to the coronal outflows case. Third, they are very transient events, disappearing together with the flare loops.

We can also rule out that the blue-shifts are directly related to the ejecta associated with the flare. First, small ejecta appear

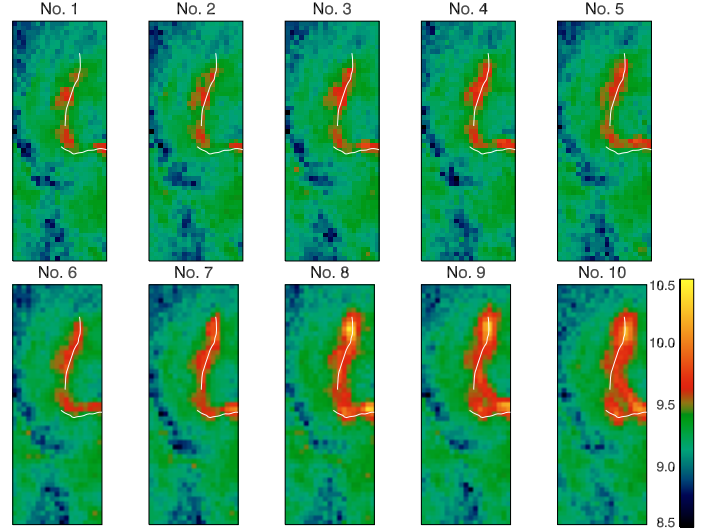


Fig. 16. Electron densities (in cm⁻³, in log-scale) from the Fe XIV 264.79/274.20 Å line ratio. The field of view is $38'' \times 102''$. The location of the ribbons is superimposed.

to lift off from the southern ribbon only, around 23:20 UT, as seen in TRACE 171 Å. Second, the ejecta are likely to be filament material, having a temperature below 1 MK, the temperature of formation of the 171 Å filter; we have no signatures of blueshifts at those temperatures in the EIS spectra. The filament ejecta have an obvious importance for the early phase of the flare, however higher cadence and sensitivity (as provided now with SDO) would be needed to study this relation.

We now examine in more detail the characteristics of the ribbon structures. We obtained electron densities from the Fe XIV 264.79, 274.20 Å line ratio, using the Fe XIV atomic calculations of Storey et al. (2000). The lines are very strong, hence accurate values are obtained. The contribution of the Si VII 274.175 Å line to the Fe XIV 274.203 Å line has been estimated from the theoretical intensity ratio with the Si VII 275.383 Å line (also included in our EIS study), predicted to be between 0.2 and 0.25 in the 10^9 – 10^{10} cm⁻³ range. The estimated Si VII contribution to the rest component of the Fe XIV 274.203 Å line is very small, of the order of 4%. Figure 16 shows the electron densities for all the EIS rasters.

These were obtained by summing the rest and blue-shifted components. The average values in the active region are about $10^{9.5}$ cm⁻³, which is typical of an active region (O’Dwyer et al. 2010). However, the ribbon structure becomes denser during the small flare, with values in the range 1 – 3×10^{10} cm⁻³. These are however lower limits, considering that the densities are averaged values of the low-lying ribbons and the foreground plasma.

We have also looked in detail at some kernels. The Fe XIV 264.79, 274.20 Å line profiles for raster No. 6, 23:16–23:20 UT, were fitted with two components, one at rest wavelength, and the other on the blue-side. Table 3 provides line intensities, widths and electron densities. Averaged densities of 6×10^9 and 1×10^{10} cm⁻³ for the rest and blue-wing components are found respectively. The density of the rest component, which corresponds to the foreground active region emission, is in excellent agreement with the density obtained from the Fe XIII 202.04, 203.83 Å ratio (5×10^9 cm⁻³), using the recent new scattering calculations of Storey & Zeppen (2010). If one assumes a unity filling factor (i.e. that the plasma is uniformly distributed along the line of sight) and estimates the emission measures for the

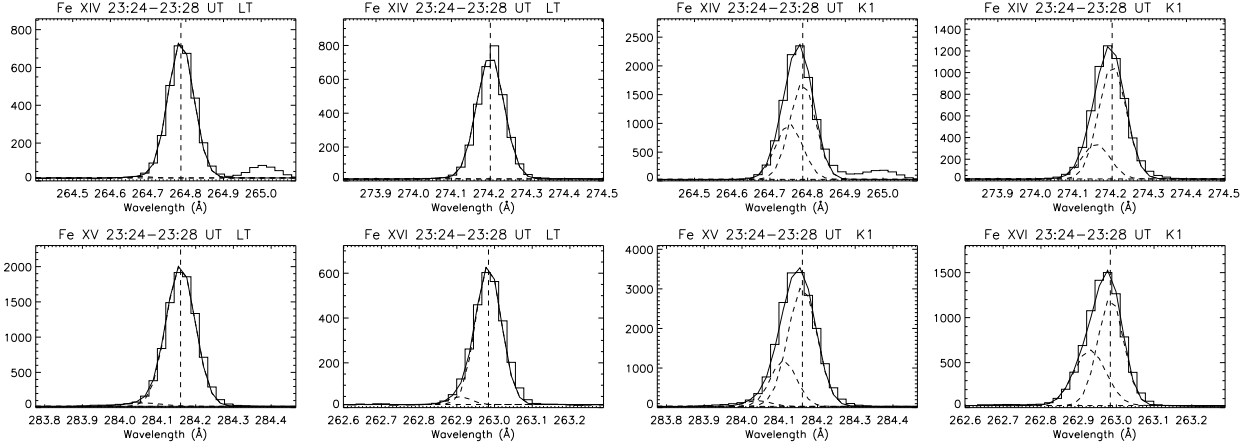


Fig. 17. *Left:* profiles of coronal lines in the LT region (see Fig. 13). *Right:* profiles of coronal lines in the K1 region, where secondary blueshifted components are shown. Ordinates are data numbers.

274.203 Å line, one obtains path lengths of 6'' and 0.3'' (200 km) for the rest and blue-wing components, respectively.

We then looked at the line profiles during the flare raster No. 8, in the loop-top (LT) and kernel (K1, K2) regions at the footpoint of the flare loop (see Fig. 13). Sample profiles for the LT and K1 regions in a few coronal lines are shown in Fig. 17. As in the previous case, the LT region is mostly foreground plasma emission, line profiles are nearly symmetric and at rest wavelengths. The density from the Fe XIV 264.79, 274.20 Å line ratios is $2 \times 10^9 \text{ cm}^{-3}$ (see Table 3).

In the Kernel K1, line profiles have a blue-wing asymmetry, more pronounced in Fe XVI, as in the previous case. It is clear that the electron density in K1 is much higher, given that the ratio of the 264.79, 274.20 Å lines is about twice the previous one, giving a density of $1.6 \times 10^{10} \text{ cm}^{-3}$. As before, we have fitted the line profiles with two Gaussians, the main one having rest wavelength. The intensity and location of the secondary component is quite uncertain, given that it depends on how accurate the rest wavelength is. For the Fe XIV, Fe XV, and Fe XVI lines, the centroid of the secondary component is shifted by 40–60 km s⁻¹ towards the blue. These are significant up-flowing velocities, considering that are just average line-of-sight projections of those along the loop structure. It is interesting to notice that, at the same footpoint location, the 10 MK Fe XXIII line profile is also blueshifted by a similar amount, as shown in Fig. 13.

The observed Fe XIV 264.79, 274.20 Å ratio of the secondary component is in the high-density limit for Fe XIV, indicating densities in excess of 10^{11} cm^{-3} . In the other kernel, K2, we obtain a density of about 10^{11} cm^{-3} . The column emission measures of the Fe XIV blue-wing components are about 10^{28} cm^{-5} , adopting photospheric abundances. If we assume a density of 10^{11} cm^{-3} , and an homogeneous plasma distribution, we obtain an estimate for the depth for the emitting material of about 10 km.

We believe that this up-flowing material is a signature of chromospheric evaporation. The question as whether a thickness of the order of 10 km is reasonable arises. The evaporation could partly be due to particle beam heating, in which case the thickness would depend upon the spectral index of the beam and the density structure of the atmosphere. However, in our hydrodynamic simulation (see below) chromospheric evaporation is being driven by a conduction front (rather than a beam) which is carrying a large amount of energy from the corona. Its associated temperature gradient is very steep, so the actual layer within which the heating/evaporation is taking place must be

located within the front and therefore be extremely narrow. As an example, the peak heat flux F_c carried by 0.1 MK electrons at a density of 10^{10} cm^{-3} traveling at the thermal speed is about $3 \times 10^7 \text{ erg cm}^{-2} \text{ s}^{-1}$. The Spitzer heat flux formula then gives an estimate for the temperature scale-length required to support this heat flux: $ds \approx (kT^{3.5})/F_c$, where k is the coefficient for thermal conduction. The length is of the order of 100 m and is a lower limit on the spatial scale. So, values of a few 100 m to a few km seem reasonable.

4. Comparison with theory: HYDRAD

We have run a numerical simulation using the hydrodynamic code: HYDRAD (Bradshaw & Mason 2003a; Bradshaw & Mason 2003b; Bradshaw & Cargill 2006) in order to examine the measured variations in the line intensities for the main flare loop in greater detail. The properties of the flaring loop (e.g. loop length, peak temperature) were determined from the observations and we aimed to match them as closely as possible in the simulation. The distance between the footpoints is about $2.5 \times 10^9 \text{ cm}$, and, without knowing the inclination, we have assumed a semi-circular loop of length $4 \times 10^9 \text{ cm}$. An initially hydrostatic loop (gravitationally stratified) having this length, a uniform temperature of 0.02 MK, and an apex density of $1.5 \times 10^9 \text{ cm}^{-3}$, was subject to uniform heating everywhere along its length for a period of 8 min. The onset time for the heating was set at 23:18 UT and the energy was deposited all along the loop (uniformly) with a rate of $0.6 \text{ erg cm}^{-3} \text{ s}^{-1}$.

We would like to point out that the initial conditions (temperature and density) do not affect at all the thermodynamic evolution of the flare. The total energy released in the heating event is orders of magnitude greater than the total energy of the pre-heated loop. Thus, the input energy from heating effectively governs its thermal properties thereafter. The energy deposited into the loop was chosen such that the loop of chosen length could be heated up to the observed peak temperature.

The evolution of the electron temperature and density (apex values) are shown in the upper two panels of Fig. 18. The temperature reaches a peak of 10 MK at 23:20 UT and maintains this value until 23:26 UT, at which time the heating is switched off. The density increases due to evaporated gas from the chromosphere, and reaches a peak of just under $4 \times 10^{10} \text{ cm}^{-3}$ between 23:26 and 23:30 UT, in excellent agreement with the value inferred from the emission measure. After 23:26 UT, when the

Table 3. Observed values from three areas.

Ion	λ_{obs} (\AA)	v (km s^{-1})	F (m\AA)	I_{obs}	N_e (cm^{-3})
No. 6 – K					
Fe XIV (rest)	264.787		40	1660	
Fe XIV (bw)	264.730 (57)		45	542	
Fe XIV (rest)	274.203		40	1310	
Fe XIV (dbl)				1255	6×10^9
Fe XIV (bw)	274.144 (65)		48	230	1×10^{10}
Fe XVI (rest)	262.984		40	971	
Fe XVI (bw)	262.926 (66)		68	703	
Fe XVI (rest)	262.984		40	1070	
Fe XVI (bw1)	262.929 (63)		45	497	
Fe XVI (bw2)	262.837 (168)		45	109	
No. 8 – LT					
Fe XIV (rest)	264.787		40	1.15×10^3	
Fe XIV (bw)	264.681		32	10	
Fe XIV (rest)	274.204		42	1.15×10^3	
Fe XIV (dbl)				1.14×10^3	2×10^9
Fe XIV (bw)	274.080		30	6	
Fe XV (rest)	284.160		45	8.3×10^3	
Fe XV (bw)	284.081		60	270	
Fe XVI (rest)	262.984		40	1.1×10^3	
Fe XVI (bw)	262.908		34	54	
Fe XXIII	263.758		70	304	
No. 8 – K1					
Fe XIV (rest)	264.787		40	2.7×10^3	
Fe XIV (bw)	264.751 (41)		42	1.6×10^3	
Fe XIV (rest)	274.204		42	1.7×10^3	
Fe XIV (dbl)				1.6×10^3	9×10^9
Fe XIV (bw)	274.160 (47)		43	5.2×10^3	$> 10^{11}$
Fe XV (rest)	284.160		45	1.26×10^4	
Fe XV (bw)	284.110 (53)		40	4.3×10^3	
Fe XVI (rest)	262.985		40	2.1×10^3	
Fe XVI (bw)	262.930 (62)		50	1.3×10^3	
Fe XXIII	263.722 (49)		90	190	

Notes. Observed wavelengths (λ_{obs}) are shown for the centroid position of the rest and blue-wing (bw) components. Values in parentheses are the corresponding velocities of the bw components towards the observer, in km s^{-1} . The full-width-half-maximum (F) of the Gaussian line profile is then shown, together with the measured intensity I_{obs} ($\text{erg cm}^{-2} \text{s}^{-1} \text{sr}^{-1}$), and the derived electron densities N_e from the Fe XIV line ratios. Rest wavelengths (\AA) are 264.787, 274.203 (Fe XIV), 284.160 (Fe XV), 262.984 (Fe XVI), 263.765 (Fe XXIII). The intensity for the deblended Fe XIV (dbl) line is given.

corona starts to cool, the evaporated material begins to drain. The extremely rapid initial cooling is due to highly efficient thermal conduction, which is clear because material continues to be evaporated into the corona after the heating is switched off. Soon after, a transition to predominantly radiative and enthalpy-driven cooling is expected (Bradshaw & Cargill 2010).

The lower panel in Fig. 18 shows the non-equilibrium population fractions of Fe XVI, Fe XVII, Fe XXIII at the loop apex. These were calculated using a new fast and efficient solver for the ionisation state described in Bradshaw (2009). This allows the non-equilibrium ionisation state for elements hydrogen through zinc to be quickly calculated for any given time-dependent temperature ($10^4 \leq T \leq 10^8$ K) and density profiles. In the present case the deviations from equilibrium are small due

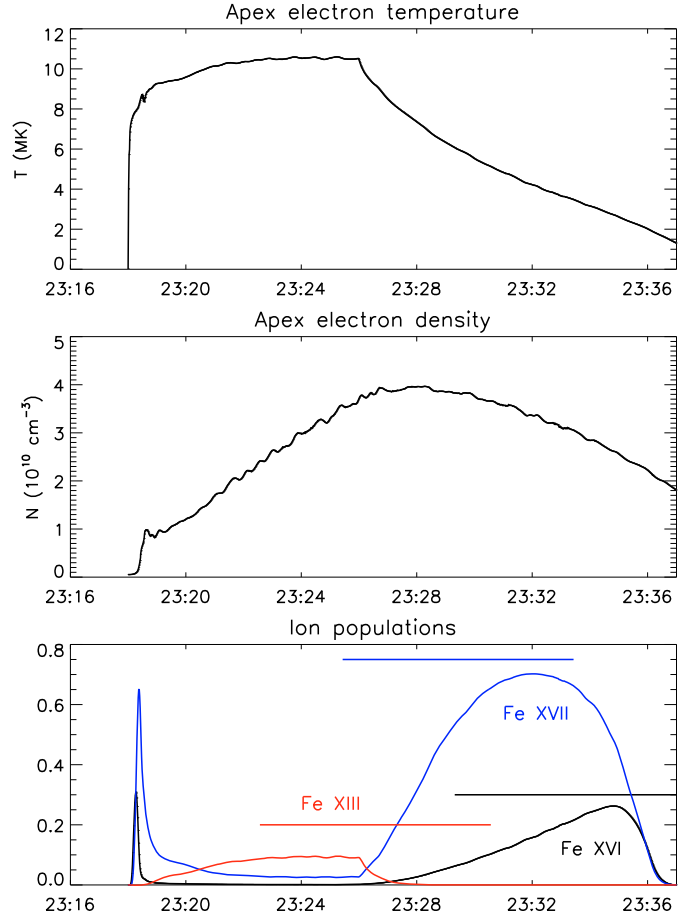


Fig. 18. The theoretical variations of the apex electron temperature (top figure) and density (middle figure). The bottom figure shows the ion populations. The horizontal bars indicate the timings of peak emission as observed with 4-min cadence by *Hinode* EIS.

to the high densities reached. The Fe XXIII population fraction is elevated between 23:20 and 23:26 UT, and becomes negligible after 23:27 UT which is consistent with significant Fe XXIII emission only being observed during the EIS raster No. 8 around 23:25 UT. The population fractions of Fe XVI and Fe XVII become elevated after 23:28 UT and hence emission from these ions would be expected at this time. The observed Fe XVII emission peaked during the EIS raster No. 9 around 23:29 UT. The observed Fe XVI emission appears to have peaked later, during the EIS raster No. 10 at around 23:33 UT. Unfortunately, no later observations are available to study the further cooling. The temporal “cadence” is only 4 min, hence only a rough comparison with the numerical simulation can be done. However, good agreement between the predicted and observed peak emission during the cooling is found.

5. Summary and conclusions

The observations presented here are an almost textbook case of a small flare, however they include a number of new features. During the early, impulsive phase, and well before any significant X-ray emission occurred, very localised kernels located in the ribbons showed significant blue-shifted emission only in lines formed between 2–3 MK, reaching values of 170 km s^{-1} along-the-line-of-sight. Brightenings in

chromospheric and lower-TR lines also occurred at the same locations, kernels in the flare ribbons.

When hot (10 MK) loop structures were observed, at their footpoints significant (40–60 km s⁻¹ along-the-line-of-sight) blue-shifted emission was observed in lines formed between 2–3 MK, and also in the hot 10 MK emission, although there is more uncertainty due to line blends. The blue-shifts disappeared with the flare loop structures, and were replaced with red-shifts.

No significant blue- or red-shifts were seen in lines formed below 2 MK, although chromospheric red-shifts cannot be ruled out because they could not be detected due to problems with line blends in He II.

Electron densities as measured from the blueshifted components of the Fe XIV line ratio in the kernels are well in excess of 10¹⁰ cm⁻³, with typical values of the order of 10¹¹ cm⁻³ or more during the peak phase at the footpoints of the flare loops. It is interesting to notice that similar values were estimated from the X-ray kernel emission from Skylab (Kahler et al. 1976). The measured densities and emission measures indicate that the high-density blue-shifted regions are at sub-resolution level (10–200 km approximately).

The strong blue-shifts primarily from the 2–3 M K plasma were somewhat surprising, although similar results were obtained from SMM (Zarro et al. 1988) and CDS (Del Zanna et al. 2002a) observations. However, in the SMM case it is difficult to establish the precise temperature of the emitting plasma, given that Mg XI is formed over a broad range of temperatures, between 1.2 and 6 MK. In the CDS case the blue-shifts were long-lasting (1 h), compared to the present observation (about fifteen minutes). The physical processes at work are possibly similar though, the difference being mostly the duration of the heating.

In the past, most attention has been devoted to blue-shifts in flare-temperature lines, however the CDS and EIS results suggest that the bulk of observable chromospheric evaporation is in lines formed between 2 and 6 MK. Future observations should take this into account.

Using a number of EIS emission lines formed over a broad temperature range we showed that the loop-top emission of the main flare loop can be explained with an isothermal temperature of 10 MK, the same temperature obtained from the GOES light curves, and the same obtained by Feldman et al. (1996) for flares of similar magnitude using the satellite lines observed by Yohkoh BCS. This suggests that assuming isothermal temperatures is a good approximation for flare loops.

In the small flare we have studied, the heating appears to last for only a few minutes. The hot 10 MK loop structures quickly cool, showing enhanced emission in progressively lower-temperature lines. The cooling process is in broad agreement with non-equilibrium HYDRAD numerical simulations which in this case, due to the high densities involved, turn out to be close to equilibrium.

With regard to the driving mechanism behind the chromospheric evaporation, we are unable to assess the relative importance of heating by a beam of non-thermal electrons or thermal conduction (due to a lack of observations from RHESSI), although the absence of strong, non-thermal 17 GHz radio emission is indicative of a weak electron beam. We would like to point out that within our HYDRAD numerical simulation, the chromospheric evaporation is solely being driven by thermal conduction. Further detailed forward-modelling of this and other flare events are on-going, to compare not only densities and temperatures but also line profiles with observations.

In this paper, we discuss which EIS spectral lines we found most useful for studies of small flares, and which lines are

particularly problematic because of blending (for a discussion of other flare lines, see Del Zanna 2008a; and Del Zanna & Ishikawa 2009). These considerations should be taken into account in future studies which use the EIS instrument.

Clearly, for an in-depth study of both the heating and cooling mechanisms in solar flares, much faster observing cadences would be required. At the same time, long exposures are required to measure the signatures of chromospheric evaporation. Also, a large number of lines needs to be observed, in particular for deblending many of the strong lines and to cover a broad temperature range. All this is at the limits of the capabilities of the EIS instrument, with restricted data transmission rates, and it provides a great challenge for any future instruments.

Acknowledgements. Support from STFC is acknowledged. *Hinode* is a Japanese mission developed and launched by ISAS/JAXA, with NAOJ as domestic partner and NASA and STFC (UK) as international partners. It is operated by these agencies in co-operation with ESA and NSC (Norway). We acknowledge making extensive use of the *Hinode* data Centre Europe (Norway), and using NoRH and TRACE data. We warmly thank C. Chifor. She was *Hinode*/EIS Chief Observer between 21 May and 1 June 2007 when she visited the JAXA/ISAS facilities in Japan. She coordinated the EIS observing plan with the XRT and SOT observing plans and with other instruments. We thank the anonymous referee for detailed and useful comments which helped to improve the manuscript.

References

- Antonucci, E., Gabriel, A. H., Acton, L. W., et al. 1982, *Sol. Phys.*, 78, 107
- Antonucci, E., Gabriel, A. H., & Dennis, B. R. 1984, *ApJ*, 287, 917
- Asplund, M., Grevesse, N., Sauval, A. J., & Scott, P. 2009, *ARA&A*, 47, 481
- Bentley, R. D., Doschek, G. A., Simnett, G. M., et al. 1994, *ApJ*, 421, L55
- Bradshaw, S. J. 2009, *A&A*, 502, 409
- Bradshaw, S. J., & Mason, H. E. 2003a, *A&A*, 401, 699
- Bradshaw, S. J., & Mason, H. E. 2003b, *A&A*, 407, 1127
- Bradshaw, S. J., & Cargill, P. J. 2006, *A&A*, 458, 987
- Bradshaw, S. J., & Cargill, P. J. 2010, *ApJ*, 710, L39
- Cheng, C., Oran, E. S., Doschek, G. A., Boris, J. P., & Mariska, J. T. 1983, *ApJ*, 265, 1090
- Chifor, C. 2008, Ph.D. Thesis, Univ. of Cambridge, UK
- Chifor, C., Hannah, I. G., Mason, H. E., et al. 2008, in *First Results From Hinode*, ed. S. A. Matthews, J. M. Davis, & L. K. Harra, ASP Conf. Ser., 397, 164
- Churilov, S. S., & Levashov, V. E. 1993, *Phys. Scr.*, 48, 425
- Culhane, J. L., Harra, L. K., James, A. M., et al. 2007, *Sol. Phys.*, 60
- Czaykowska, A., de Pontieu, B., Alexander, D., & Rank, G. 1999, *ApJ*, 521, L75
- Del Zanna, G. 2008a, *A&A*, 481, L69
- Del Zanna, G. 2008b, *A&A*, 481, L49
- Del Zanna, G. 2009a, *A&A*, 508, 501
- Del Zanna, G. 2009b, *A&A*, 508, 513
- Del Zanna, G. 2010, *A&A*, 514, A41
- Del Zanna, G., & Mason, H. E. 2005, *A&A*, 433, 731
- Del Zanna, G., & Ishikawa, Y. 2009, *A&A*, 508, 1517
- Del Zanna, G., Gibson, S. E., Mason, H. E., Pike, C. D., & Mandrini, C. H. 2002a, *Adv. Space Res.*, 30, 551
- Del Zanna, G., Landini, M., & Mason, H. E. 2002b, *A&A*, 385, 968
- Del Zanna, G., Berrington, K. A., & Mason, H. E. 2004, *A&A*, 422, 731
- Del Zanna, G., Chidichimo, M. C., & Mason, H. E. 2005, *A&A*, 432, 1137
- Del Zanna, G., Berlicki, A., Schmieder, B., & Mason, H. E. 2006a, *Sol. Phys.*, 234, 95
- Del Zanna, G., Schmieder, B., Mason, H., Berlicki, A., & Bradshaw, S. 2006b, *Sol. Phys.*, 239, 173
- Del Zanna, G., Storey, P. J., & Mason, H. E. 2010, *A&A*, 514, A40
- Dere, K. P., Landi, E., Young, P. R., et al. 2009, *A&A*, 498, 915
- Doschek, G. A., & Warren, H. P. 2005, *ApJ*, 629, 1150
- Doschek, G. A., Kreplin, R. W., & Feldman, U. 1979, *ApJ*, 233, L157
- Doschek, G. A., Warren, H. P., Mariska, J. T., et al. 2008, *ApJ*, 686, 1362
- Feldman, U., Doschek, G. A., Behring, W. E., & Phillips, K. J. H. 1996, *ApJ*, 460, 1034
- Fisher, G. H. 1987, *ApJ*, 317, 502
- Fisher, G. H., Canfield, R. C., & McClymont, A. N. 1985a, *ApJ*, 289, 425
- Fisher, G. H., Canfield, R. C., & McClymont, A. N. 1985b, *ApJ*, 289, 414
- Fujiki, K. 1997, Ph.D. Thesis, The Graduate University of Advanced Studies
- Hanaoka, Y. 1999, in *Proceedings of the Nobeyama Symposium*, ed. T. S. Bastian, N. Gopalswamy, & K. Shibasaki, 153
- Hara, H., Watanabe, T., Harra, L. K., et al. 2008, *ApJ*, 678, L67

- Harra, L. K. 2008, *Int. J. Mod. Phys. D*, 17, 693
- Haugan, S. V. H. 1997, SOHO CDS software note, 47
- Kahler, S. W., Krieger, A. S., & Vaiana, G. S. 1975, *ApJ*, 199, L57
- Kahler, S. W., Petrasso, R. D., & Kane, S. R. 1976, *Sol. Phys.*, 50, 179
- Kano, R., Sakao, T., Hara, H., et al. 2008, *Sol. Phys.*, 249, 263
- Ko, Y., Doschek, G. A., Warren, H. P., & Young, P. R. 2009, *ApJ*, 697, 1956
- Mariska, J. T., Emslie, A. G., & Li, P. 1989, *ApJ*, 341, 1067
- Mason, H. E., Shine, R. A., Gurman, J. B., & Harrison, R. A. 1986, *ApJ*, 309, 435
- Milligan, R. O., & Dennis, B. R. 2009, *ApJ*, 699, 968
- Nakajima, H., Nishio, M., Enome, S., et al. 1994, *IEEE Proc.*, 82, 705
- O'Dwyer, B., Del Zanna, G., Mason, H. E., et al. 2010, *A&A*, 525, A137
- Peter, H. 2010, *A&A*, 521, A51
- Raftery, C. L., Gallagher, P. T., Milligan, R. O., & Klimchuk, J. A. 2009, *A&A*, 494, 1127
- Redfors, A. 1988, *Phys. Scr.*, 38, 702
- Sterling, A. C., Chifor, C., Mason, H. E., Moore, R. L., & Young, P. R. 2010, *A&A*, 521, A49
- Storey, P. J., & Zeippen, C. J. 2010, *A&A*, 511, A78
- Storey, P. J., Mason, H. E., & Young, P. R. 2000, *A&AS*, 141, 285
- Tsuneta, S., Ichimoto, K., Katsukawa, Y., et al. 2008, *Sol. Phys.*, 249, 167
- White, S. M., Thomas, R. J., & Schwartz, R. A. 2005, *Sol. Phys.*, 227, 231
- Young, P. R., Del Zanna, G., Mason, H. E., et al. 2007, *PASJ*, 59, 857
- Zarro, D. M., Slater, G. L., & Freeland, S. L. 1988, *ApJ*, 333, L99